Progressive alterations in polysomal architecture in a mouse model of Huntington's disease

Eva Martin-Solana[1], Irene Diaz-Lopez[2], Ivan Ventoso[3], Jose-Jesus Fernandez[1,4,5,*], Maria Rosario Fernandez-Fernandez[1,4,5,*]

[1] Centro Nacional de Biotecnología (CNB-CSIC). Campus UAM, Darwin 3, 28049 Madrid, Spain.

[2] MRC Laboratory of Molecular Biology. Cambridge Biomedical Campus, Cambridge, UK

[3] Centro de Biología Molecular "Severo Ochoa" (CSIC-UAM) and Departamento de Biología Molecular, Universidad Autónoma de Madrid (UAM). Madrid, Spain.

[4] Centro de Investigación en Nanomateriales y Nanotecnología (CINN-CSIC). Av. Vega 4-6, 33940 El Entrego, Asturias, Spain.

[5] Instituto de Investigación Sanitaria del Principado de Asturias (ISPA). Av. Hospital Universitario s/n, 33011 Oviedo, Asturias, Spain.

[*] Corresponding authors:

JJ.Fernandez@csic.es, MR.Fernandez@csic.es

Abstract

Given their highly polarized morphology and functional singularity, neurons require precise spatial and temporal control of protein synthesis. Alterations in protein translation have been implicated in the development and progression of a wide range of neurological and neurodegenerative disorders, including Huntington's disease (HD). We examined the architecture of polysomes in their native brain context by performing 3D electron tomography of striatal tissue from the zQ175 knock-in mouse model of HD. Results revealed progressive remodelling towards a more compacted polysomal architecture, an effect that coincided with the emergence and progression of HD related symptoms. This aberrant architecture is compatible with ribosome stalling phenomena. In fact, we also detected an increase in the striatal expression of the stalling relief factor *EIF5A2*. Polysomal sedimentation gradients showed a significant increase in the accumulation of free 40S ribosomal subunits in zQ175 striatal samples. Together, these findings indicate that changes in the architecture of the protein synthesis machinery may underlie translational alterations associated with HD, thus opening new avenues for understanding the progression of this disease.

Introduction

Huntington's disease (HD) is a genetically inherited dominant neurodegenerative disorder caused by expansion of a CAG repeat sequence in the coding sequence of huntingtin protein (HTT) (Bates, 2005). Symptoms manifest at middle age (35-45 years) and life expectancy after disease onset is usually 15–20 years. Initially, the disease primarily affects the corpus striatum, and neurodegeneration selectively affects medium-sized spiny neurons (MSSNs), which are GABAergic projection neurons (Albin *et al*, 1992; Vonsattel *et al*, 1985). HD patients develop progressive motor dysfunction, cognitive decline, and psychological alterations (Bates *et al*, 2015; Ross & Tabrizi, 2011). Although different pharmacological approaches are being explored, there is no effective treatment for the disease (Caron *et al*, 2018; Tabrizi *et al*, 2019). Recently, promising clinical trials of therapies based on antisense oligonucleotides were halted in phase III, as the potential benefits did not outweigh the risks (Kwon, 2021).

The CAG repeat is polymorphic in normal chromosomes and is expanded in HD-mutated chromosomes (The Huntington's Disease Collaborative Research Group, 1993). The number of repeats influences the age of onset and disease severity. The repeat is located in exon 1 and encodes a polyglutamine sequence (polyQ) that resides in the N-terminal region of the protein. The polyQ sequence in HTT is followed by a proline rich domain (PRD) that is also polymorphic in the human population (Saudou & Humbert, 2016). HTT is a large 348-kDa protein with a considerable degree of conservation from flies to mammals (Saudou & Humbert, 2016). However, exon 1 is less evolutionarily conserved than other exons. Interestingly, the PRD is found only in mammals, suggesting recent evolution of the HTT protein (Tartari *et al*, 2008). In yeast systems the presence of the PRD reduces the toxicity of exon 1 constructs containing polyQ sequences in the pathological range (Duennwald *et al*, 2006), and also reduces the rate of polyQ aggregation *in vitro* (Bhattacharyya *et al*, 2006; Dehay & Bertolotti, 2006; Yang *et al*, 2016; Meriin *et al*, 2007). Normal

HTT function and the basis for the toxic effects of mutant HTT (mHTT) in the context of HD are still not fully understood (Nowogrodzki, 2018).

As a consequence of their polarized organization and the particularities of synaptic activity, neurons require precise spatial and temporal control of protein translation, and are therefore particularly susceptible to alterations in the mechanisms controlling protein translation (Kapur *et al*, 2017). Dysregulation of cellular mechanisms involved in protein synthesis has been widely implicated in the development and progression of diverse neurological and neurodegenerative diseases (Darnell, 2014; Gao *et al*, 2017; Kapur & Ackerman, 2018; Kapur *et al*, 2017). Specifically, several studies have shown that mutations in proteins involved in resolving ribosome stalling induce motor dysfunction, neurodegeneration (Chu *et al*, 2009), and neuronal cell death in mice (Ishimura *et al*, 2014). A growing body of evidence points to alterations in mHTT translation and in overall protein synthesis in the context of HD. Surprisingly, mRNAs containing expanded CAG repeats are translated more efficiently than those in the non-pathological range (Krauß *et al*, 2013). A higher number of CAG repeats favours the binding of a translation regulation complex containing MID1-PP2A. Consequently, the accumulation of mHTT protein is considerably greater than that of non-pathological HTT. These results reveal an interesting gain of function of the mutant protein at the mRNA level (Krauß *et al*, 2013). Several research groups have evaluated translation in the context of HD using the SUnSET method, with conflicting findings. The method is based on the ability of puromycin to label newly synthesized peptides when administrated at low doses. On the one hand, Creus-Muncunill *et al*. reported an increase in puromycin incorporation into striatal cells in brain slices from the R6/1 HD mouse model (Creus-Muncunill *et al*, 2019), suggesting that protein translation is increased and that an overall increase in protein translation could constitute a novel pathogenic mechanism in HD. Interestingly, proteomic characterization revealed that the increase in translation specifically affected a set of proteins involved in ribosomal and oxidative phosphorylation, while other proteins implicated in neuronal structure and function were downregulated. On the other hand, Joag *et al.* reported reduced incorporation of puromycin into *Drosophila* cells overexpressing a fragment of HTT containing a 138 polyQ expansion

(Joag *et al*, 2020). These results were also reproduced in SYS5 and Neuro2a cells and suggest that expression of a pathogenic mHTT fragment induces a deficit in protein synthesis. Similarly, a recent study reported reduced incorporation of puromycin in heterozygous and homozygous ST*Hdh* cell lines generated from a knock-in mouse model containing 111 CAGs as compared with wild type (WT) counterparts (7 CAGs), suggesting reduced protein synthesis in HD (Eshraghi *et al*, 2021). HTT was proposed to promote ribosome stalling through binding to ribosomes, an effect that is exacerbated by mHTT (Eshraghi *et al*, 2021). Interestingly, yeast cells expressing fragments of pathogenic exon 1 show downregulation of expression of genes implicated in ribosome biogenesis and rRNA processing and metabolism (Tauber *et al*, 2011), and hence general repression of protein synthesis. The discrepant findings described above may well be due to the different HD models used, or may be representative of distinct disease scenarios. Overall, these results point to dysregulation of protein synthesis in the presence of mHTT.

Electron tomography allows the study of the 3D subcellular architecture and the organization of molecules in their native cellular or tissue environment with nanometric resolution (Frank, 2006; He & Fernández, 2010). It is based on the acquisition of images from a sample at different tilt angles that are subsequently processed and combined to yield a 3D reconstruction or tomogram (Fernandez, 2012). Multiple studies have employed electron tomography to investigate the spatial distribution and interaction of ribosomes in their native cellular context in bacteria (Brandt *et al*, 2009), isolated glioblastoma cells (Brandt *et al*, 2010), and HeLa cells (Mahamid *et al*, 2016), and more recently as a proof of principle in tissue in *Caenorhabditis elegans* (Schaffer *et al*, 2019). Rapid-freezing techniques are used to ensure optimal structural preservation of cells and tissues for electron tomography. Specifically, high-pressure freezing (HPF) is used to fully vitrify bulk specimens (up to 200–400 μm thick) through synchronized pressurization and cooling of the sample within milliseconds. Tissue samples can either be processed for observation under cryogenic conditions (Schaffer *et al*, 2019) or freeze-substituted to replace the frozen cellular water with organic solvents and embedded in resins at low temperature to proceed with the analysis at room temperature (He & Fernández, 2010;

Fernandez-Fernandez *et al*, 2017). While fully cryogenic conditions are ideal to preserve the structure in closest-to-native conditions and to achieve the maximum structural resolution, these protocols are not yet used routinely (Schaffer *et al*, 2019). Thus, HPF and FS is the combination of choice for systematic comparative analysis of ultrastructural tissue alterations in pathological conditions (Fernandez-Fernandez *et al*, 2017).

In the present study, we explored the architecture of neuronal polysomes in their native brain context using 3D electron tomography of HPF/FS striatal tissue obtained from the zQ175 knock-in HD mouse model (Menalled *et al*, 2012). We observed progressive remodelling of polysomal architecture resulting in a densely packed conformation compatible with ribosome stalling phenomena. Supporting this hypothesis, we observed increased expression of the stalling release factor *EIF5A2* in HD striatal samples, as well as limited recruitment of the factor to polysomes, suggesting inefficient release of ribosome stalling. Furthermore, polysomal sedimentation gradients revealed a remarkable increase in the accumulation of free 40S ribosomal subunits in striatal samples from HD mice. These changes in the architecture of the protein synthesis machinery may constitute the basis of translational alterations associated with HD. Together, our findings open new avenues to better understand the role of protein translation in disease progression and facilitate the search for potential therapeutic targets.

Materials and Methods

Animals

A stable colony of the zQ175 mice (Menalled *et al*, 2012) was established using founders donated by the Cure Huntington's Disease Initiative (CHDI) and obtained from Jackson Laboratory Inc. The zQ175 line is a knock-in line bred on a C57BL/6J background with an endogenous murine *HTT* gene containing a chimeric human/mouse exon 1 with approximately 190 CAG repeats (B6.12951-Htt<tm1Mfc<190JChdi). Heterozygous mice and controls were bred as a stable colony in the animal facility of the Centro Nacional de Biotecnología, Madrid, and provided with food and water *ad libitum*. All experiments complied

with Spanish and European legislation and Spanish National Research Council (CSIC) ethics committee on animal experimentation.

Sample preparation based on HPF/FS for electron microscopy

Brain tissue samples were prepared for electron microscopy (EM) and tomography following our protocols for optimal structural preservation based on high-pressure freezing and freeze-substitution (HPF/FS), as previously described (Fernandez-Fernandez *et al*, 2017). In short, mouse brains were dissected immediately post-mortem and 200-µm-thick sagittal slices were cut using a tissue slicer (Stoelting, Co.). Striatal samples were promptly extracted, placed on a flat specimen carrier, and frozen under high-pressure in a Leica EMPACT2 device. The samples were further processed with freeze-substitution of frozen water to methanol and embedded in Lowicryl resin HM20 with a Leica AFS2 EM FSP system. Sections (250 nm) were obtained from the resin-embedded samples using a Leica Ultracut EM-UC6 ultramicrotome, and placed on Quantifoil S7/2 grids.

Electron microscopy

A conventional JEOL JEM-1011 electron microscope (100 kV) was used to screen the 250-nm-thick sections, check the integrity of the tissue samples, and select areas of interest. An average of 5 EM grids, each containing 4 sections, were examined per animal. Animals of 2, 8, 10, and 11 months of age were analysed. Cells compatible with striatal medium-sized spiny neurons were selected based on morphological criteria (Matamales *et al*, 2009) (Figure EV1) and representative cytoplasmic areas with abundant ribosomes were selected for subsequent 3D studies with ET.

Electron tomography

Tomographic data were acquired by taking series of images from the sections while tilting them within a range of ±60° at 1° intervals around a single tilt-axis. The tilt-series were acquired using a Thermo Fisher Scientific Talos Arctica electron microscope (200 kV) equipped with a Falcon II electron direct detector

or using a FEI Tecnai G2 (200 kV) equipped with a CCD camera. The pixel size at the specimen level was 0.37 nm and 0.59 nm, respectively. For processing, visualization and analysis, images were rescaled with a binning factor of 4. Prior to ET, grids were incubated in a solution of 10-nm diameter colloidal gold (EM.BSA 10, Electron Microscopy Sciences, Hatfield, PA, USA) to facilitate subsequent image alignment.

Tilt-series alignment and calculation of the 3D tomograms were conducted using IMOD standard software (Kremer *et al*, 1996), applying standard protocols (Fernandez, 2012). Images of the tilt-series were mutually aligned using the colloidal gold beads as fiducial markers. Tomograms were reconstructed with the standard method, weighted back-projection (WBP), using a filter that simulates an iterative reconstruction method (SIRT) (Fernandez, 2012).

Computational analysis of the ribosomal pattern in tomograms

To characterize the ribosomal pattern observed in the tomograms, we developed computational procedures to (1) automatically identify ribosomes and (2) examine how they are organized. The procedure for ribosome identification is based on the Laplacian of Gaussian (LoG), a strategy commonly used in the field of computer vision to detect 'blobs' (Nixon and Aguado, 2020). Here, we extended this strategy to 3D in order to work with tomograms. Essentially, the procedure applies Gaussian filtering, with a standard deviation related to the size of the target 3D blob (i.e. the ribosome, around 25 nm in diameter) and, afterwards, a Laplacian operator (i.e. second-order derivative) is applied to the Gaussian-filtered tomogram. The peaks in the resulting LoG map correspond to positions at which ribosomes are located in the tomogram. The final ribosome positions are extracted using a segmentation operation based on thresholding of the LoG map.

To analyse ribosomal organization based on the detected ribosome positions, we implemented second-order spatial point pattern analysis techniques extended to 3D. Specifically, we used Ripley's K function (Ripley, 1988), $K(r)$, which allows us to measure the expected number of ribosomes within a

distance *r* from an arbitrary ribosome, normalized by the density of the ribosome distribution. This function can be mathematically expressed as follows:

$$K(r) = V \cdot \frac{\sum_{i=1}^{n} \sum_{j \neq i} e_i(r) \cdot I\left[d_{ij} \leq r\right]}{n^2}$$

where *V* is the volume of the tomogram, *n* denotes the number of ribosomes in the tomogram, d_{ij} represents the Euclidean distance from the ribosome *i* to *j*, *I[.]* is an indicator function that equals 1 if the distance d_{ij} is within the radius *r,* and otherwise equals 0. The term $e_i(r)$ is an edge-correction factor to properly weight the contribution of ribosomes with partial neighbourhood due to their proximity to the edge of the tomogram (Ripley, 1988). Ripley's K function is calculated at a range of distances *r*, with a recommended maximum value that should be lower than half of the shortest dimension of the sample domain (Ripley, 1988; Baddeley *et al*, 1993). In this work, the spatial analysis was applied at distances ranging from 25 nm (i.e. ribosome diameter) to 100 nm.

Under the hypothesis of complete spatial randomness (CSR), the K function is equal to the volume of a sphere of radius *r* (Ripley, 1988; Baddeley *et al*, 1993): $K_{CSR}(r) = 4/3 \cdot \pi \cdot r^3$. The ratio $K(r)/K_{CSR}(r)$ thus allows analysis of the ribosomal distribution pattern and its classification into the three main categories (Diggle, 2013): aggregation or clustering (if $K(r)/K_{CSR}(r) > 1$); regularity or dispersion (if $K(r)/K_{CSR}(r) < 1$); or random (if $K(r)/K_{CSR}(r) = 1$). Supplementary Figure S1 illustrates the calculation of Ripley's K function and the three main spatial distribution patterns.

Analysis of the ribosomal distribution was applied to selected tomograms from 11-month-old animals, acquired on a FEI Tecnai G2 microscope. The larger field of view of this microscope allowed acquisition of regions with an area up to 2.4 µm x 2.4 µm.

qRT-PCR

Striatal samples from 12-month-old mouse brains were used for gene expression analysis (8 heterozygous zQ175 animals and 8 corresponding matched WT controls). The following genes were analysed: *EIF5A1*, *EIF5A2*,

DHPS, and *DOHH.* The primers used are described in Supplementary information (Table 1). Reference genes were used for normalization of gene expression data (*GAPDH*, *BACT*, *B2M*, *18S,* and *YWHAZ* (primers in Supplementary information, Table 2). The suitability of reference genes for normalization of gene expression was evaluated using Normfinder algorithm, which showed that *YWHAZ* was the most stable and accurate gene for normalization. Total RNA was isolated using the Maxwell 16 LEV simply RNA tissue kit (Promega, #AS1280), and RNA integrity was assessed using the Agilent 2100 Bioanalyzer. RIN values ranged from 7 to 9.9, indicating a very high level of sample integrity. cDNA synthesis was performed using the iScript cDNA Synthesis kit (Bio-rad, #170-8891). qRT-PCR was performed in triplicate on a CFX384 Real Time System C1000 Thermal Cycler (Bio-rad) using Sso Fast EvaGreen Supermix (Bio-rad, #172-5204). Reactions included a non-template control and primer efficiency curves were generated. ValidPrime kit (TATAA Biocenter, #A105S10) was used as control for genomic background (gDNA). The contribution of gDNA to qPCR signal was less than 6.5% in all cases. A melting curve from 60°C to 95°C (0.5°C/seg) was included at the end of the program to verify the specificity of the PCRs. Data processing was carried out using GenEx v5.4.4 (MultiD Analysis AB, Gothenburg, Sweden). The $2^{-\Delta(\Delta Cq)}$ method was used to calculate the relative fold change in gene expression of samples normalized to *YWHAZ* gene expression (Livak & Schmittgen, 2001).

Cell culture and transfection

HEK293T cells were cultured in DMEM medium (Sigma, #D6429) supplemented with 10% inactivated foetal bovine serum, non-essential amino acids (1:100, Sigma, #M7145), 0.5 μg/ml amphotericin B (Fungizone™) (Gibco™, #15290018), penicillin-streptomycin (1:100, Sigma, #P4333), and 50 μg/ml gentamycin (Sigma, #G1397). Cells were cultured at 37ºC in a 5% CO_2 atmosphere.

pEGFP-Q23 and pEGFP-Q74 plasmids were a gift from David Rubinsztein (Addgene plasmid # 40261 and 40262) (Narain *et al*, 1999). These express a

GFP protein fused to the sequence encoded by part of human *HTT* exon1. Fusion proteins contain either a non-pathological polyQ repeat (23Q) or a polyQ repeat in the pathological range (74Q). These plasmids were co-transfected with pCMV-NP (a plasmid expressing the influenza virus nucleoprotein) as a transfection control (Coloma *et al*, 2009).

The day before transfection 6×10^5 cells were plated per well in a M6 plate (Falcon, # 353046) to obtain 70-80% confluence. For actual transfection, plasmids were diluted in a solution containing 250 mM $CaCl_2$ to achieve a final amount of 1 or 3 μg per well (final volume per well: 3 ml) for *HTT* plasmids and 2 μg for pCMV-NP. The DNA/$CaCl_2$ solution was mixed for 1 min with an equal volume of filtered HBS buffer (50 mM HEPES pH 7.05, 1.5 mM Na_2HPO_4, 140 mM NaCl). Cells were harvested in the culture medium after the corresponding period of incubation and centrifuged at 210 *g* for 5 min at 4ºC. The pellet was then washed with PBS1x and centrifuged as before. The pellet was frozen and stored at -80ºC. Cell lysis was achieved by thermal shock (3 cycles of 15 min at RT+ 30 min at -80ºC) in a buffer containing 50 mM Tris-HCl pH 7.4 and 150 mM NaCl. The lysate was centrifuged at 16,100 *g* for 10 min at 4ºC and the supernatant used for Western-blot analysis as described below. Before recovery of the cells, the plates were observed under a Leica DMI6000B microscope at 10x magnification for the detection of GFP-fused proteins.

Polysome sedimentation gradients

Polysome profiles were generated as previously described (Heiman *et al*, 2008; Nielsen, 2011; Díaz-López *et al*, 2019), with some modifications. Briefly, the brain regions of interest (striatum) were dissected and immediately frozen in liquid nitrogen. Samples from mice of the same genotype were pooled to overcome the limitation of the low sample weight (4 mice per genotype). Frozen samples were ground with a mortar and pestle under liquid nitrogen and homogenized in ice-cold polysome extraction buffer (20 mM HEPES pH 7.4, 150 mM KCl, 5 mM $MgCl_2$, 0.5 mM DTT, 1% Triton X-100, 200 μg/ml cycloheximide [CHX], heparin 20 μg/ml, and 40 U/ml RNase inhibitor [New England Biolabs, Cat. no. M0307S]) using a potter homogenizer (10–12 strokes). After three passages through a 23G needle, the homogenates were

centrifuged at 2000 *g* for 5 min at 4ºC. The supernatants were subsequently centrifuged twice at 16,100 *g* for 10 min at 4ºC. The final supernatants (600 μl) were loaded onto 10–50% continuous sucrose density gradients in polysome buffer (20 mM HEPES pH 7.4, 150 mM KCl, 5 mM $MgCl_2$) (Gradient Master™, BioComp) and centrifuged in an SW40Ti swing-out rotor (Beckman Coulter) at 250,000 *g* for 2 h at 4ºC. Fractions (1 ml) were collected using a density gradient fractionation system (ISCO) with continuous monitoring of absorbance at 254 nm.

Polysomal sedimentation gradients of transfected cells were performed as previously described (Pringle *et al*, 2019), with some modifications. Briefly, 24 h post transfection, HEK293T cells were treated with 100 µg/ml CHX for 3 min at 37°C. Cells were then washed 3 times with cold CHX (100 µg/ml) in PBS (1x), harvested with residual CHX/PBS and centrifuged at 1000 *g* for 5 min at 4°C. The cell pellet was washed with ice-cold CHX/PBS, centrifuged at 1000 *g* for 5 min at 4°C and resuspended in 500 µl of polysome extraction buffer (100 µg/ml CHX without heparin). The cell lysate was mixed through a 23G needle and incubated on ice for 10 min (vortexing every 2-3 min). The homogenates were centrifuged at 2000 *g* for 5 min at 4ºC and subsequently centrifuged twice at 16,100 *g* for 10 min at 4ºC. The final supernatants (400 µl) were loaded onto a 10–50% continuous sucrose density gradient (Gradient Station™, BioComp) and centrifuged in an SW40Ti swing-out rotor at 250,000 *g* for 2 h at 4ºC. Fractions (1 ml) were collected manually.

Western-blot analysis

Bulk striatal samples were processed for Western-blot as described previously (Fernandez-Fernandez *et al*, 2011): 7 12-month old heterozygous animals and 7 corresponding WT controls were used. Samples were loaded onto NuPAGE 12% Bis-Tris gels (Invitrogen, NP0343) and run in MES running buffer (Invitrogen, NP0002). Proteins were transferred to nitrocellulose membranes (BioRad, 1620112). Membranes were incubated with the following antibodies: anti-hypusine (ABS1064, Merck), anti-eIF5A1 (SAB1402762, Sigma-Aldrich, Merck), and anti-eIF5A2 (GTX116635, Genetex).

Fractions from sucrose gradients were loaded and transferred as described above. Membranes were incubated with the following primary antibodies: anti-RPS6 (Elabscience, E-AB-32813), anti-RPL7 (Elabscience, E-AB-32805), and anti-hypusine (Creative Biolabs, PABL-202). For accurate quantitative comparisons membranes were first incubated with anti-RPS6 antibody. After completing the Western-blot, membranes were consecutively incubated with anti-RPL7 antibody. For this reason the residual signal of anti-RPS6 antibody is visible in images of the RPL7 signal.

Samples from transfected HEK293T cells were processed as shown above and membranes were incubated consecutively with anti-GFP (Genetex #GTX113617) and anti-NP (Coloma *et al*, 2009).

The secondary antibodies used were AffiniPure Goat anti-rabbit IgG (H+L) (Jackson ImmunoResearch, 111-035-003) and AffiniPure Goat anti-mouse IgG (H+L) (Jackson ImmunoResearch, 115-035-003). All antibodies were used at 1:1000 dilutions. The peroxidase reaction was developed with Clarity™ Western ECL substrate (Bio-Rad, 1705061). Imaging was performed using either an Odyssey Fc imaging system (Li-Cor) (quantified using Image StudioTM software) or a Molecular ChemiDoc™ Touch Imaging System (Bio-Rad) (quantified using Image Lab 6.0.1 software).

Statistical analysis

Statistical analyses were performed using GrapPad Prism 8. Normal distribution of the data was assessed using the Shapiro-Wilk test. A two-tailed unpaired Student t-test was used to compare normal distributed data (after assessing the equality of variances using Levene's test and/or Welch's correction). For non-normally distributed data, values were compared using the Mann-Whitney test for non-parametric samples. The level of significance was set at $p<0.05$. All data are presented as mean ± SD, with the exception of Figure 5D (mean ± standard error of the mean (SEM), although these data were not statistically analysed due small sample size [n=2]).

Results

Ribosomal/polysomal organization is altered in medium-sized spiny neurons in the striatum of zQ175 mice

HD involves the selective degeneration of striatal MSSNs. Therefore, we examined the architecture of the protein synthesis machinery in its native cellular context, using electron tomography to identify and characterize alterations in these neurons.

Brain tissue samples from HD animal models (heterozygous zQ175) at different ages (2, 8, 10, and 11 months) and the corresponding controls were prepared with HPF/FS for electron microscopy and tomography, as described in the Materials and Methods. This preparation protocol ensures optimal structural preservation of tissue samples. Conventional bidimensional (2D) electron microscopy of 250-nm-thick sections was used to confirm sample integrity and select areas of interest. Representative cytoplasmic areas were selected from the soma of cells compatible with striatal MSSNs where ribosomal and polysomal crowding was identified, and examined by electron tomography to determine 3D volumes.

Figures EV2 and EV3 show representative EM images and slices of 3D volumes obtained from a WT control and a zQ175 heterozygous mice at advanced age (11 months). In WT samples ribosomes are abundant, are continuously distributed across the entire cytoplasm, and form polysomal clusters in which individual ribosomes can be clearly identified. By contrast, ribosomal density is reduced in the zQ175 model and the polysomes form sparse clusters of tightly-coupled ribosomes with large areas of empty cytoplasmic space between the clusters. Figure 1 shows representative tomographic slices from animals at different ages: the distinctive pattern in HD mice becomes more pronounced with age. Together, these results indicate that remodelling of polysomal architecture in HD begins at ages (8 months) when some of the relevant phenotypes of this model (diminished rotarod performance, striatal atrophy) (Menalled *et al*, 2012) become apparent. Moreover, these alterations in polysomal architecture show a clear age-related progression.

To conduct an objective quantitative analysis, we developed a methodology for automated identification of ribosomes in tomograms followed by a second-order spatial analysis using Ripley's K function, as described in the Materials and Methods. Figures EV2D and EV3D depict the detection of ribosomes in respective tomograms from WT controls and zQ175 mice. These images show that the cytoplasm in WT animals is densely populated with ribosomes whereas in zQ175 mice the ribosomes are organized in groups.

Spatial analysis was applied to the ribosome positions in selected tomograms (5 WT and 6 heterozygous zQ175) of different neurons from 11-month-old animals (Figure EV4). Ripley's K-function $K(r)$ estimates the number of ribosomes around an arbitrary ribosome within a distance r, normalized by ribosomal density. The plots in Figure 2 depict Ripley's K-function relative to a random distribution ($K(r)/K_{CSR}(r)$, see Materials and Methods). Thus, a unit value indicates a random distribution whereas values >1 imply clustering. The functions show that the ribosomes are significantly more clustered in the heterozygous HD model ($K(r)/K_{CSR}(r)$ much higher than 1) than in WT controls, especially within shorter distances (up to 50 nm). The WT phenotype also shows some ribosome clustering, though much less pronounced than in the HD model. This is consistent with the fact that ribosomes form polysomes to ensure efficient translation. We also calculated ribosomal density (number of detected ribosomes per volume unit), which was higher in WT controls than the HD model (4955 vs. 2623 ribosomes/μm^3). The results of this objective analysis therefore reflect in quantitative terms the lower ribosomal density and more compact ribosomal clustering observed in the tomograms, corroborating the ribosomal alterations that occur in the zQ175 model.

The eIF5A2 stalling relief factor gene is overexpressed in the striatum of heterozygous zQ175 mice

The polysomal architecture phenotype of the zQ175 model is reminiscent of ribosome stalling phenomena. It is well established that the presence of consecutive prolines in a polypeptide, as occurs in the PRD region of HTT, induces ribosome stalling. Proline is neither a good donor nor a good acceptor

during peptide bond formation, as the reactive amine is embedded in the cyclic lateral chain, thus reducing its nucleophilicity (Wohlgemuth *et al*, 2008; Pavlov *et al*, 2009; Melnikov *et al*, 2016). eIF5A and its homologue in bacteria, EF-P, have been shown to participate in stimulating peptide bond formation between consecutive prolines, thereby releasing ribosome stalling (Doerfel *et al*, 2013; Gutierrez *et al*, 2013; Ude *et al*, 2013).

eIF5A is encoded by two distinct genes, giving rise to two different homologous proteins: eIF5A1 and eIF5A2 (Wu *et al*, 2020). While eIF5A1 is widely expressed in all tissues, eIF5A2 is weakly expressed in the majority of tissues with the exception of the brain and testis, where high levels are detected (Clement *et al*, 2006). eIF5A proteins are the only known proteins containing the aminoacid hypusine, formed by a posttranslational modification of lysine. The role of eIF5A in releasing ribosome stalling is dependent on hypusine (Melnikov *et al*, 2016; Saini *et al*, 2009; Schmidt *et al*, 2016). Formation of hypusine involves two enzymatic reactions (Park *et al*, 1981; Schmidt *et al*, 2016): deoxyhypusine synthase (DHS) produces deoxyhypusine, which is then hydroxylated by deoxyhypusine hydroxylase (DOHH) to produce hypusine. We investigated whether activation of the eIF5A pathway may be specifically induced in zQ175 mice. Using qRT-PCR, we analysed the expression of eIF5A factors and related genes in the striatum of 12-month old zQ175 mice and corresponding WT controls. As shown in Figure 3A, we observed no significant difference in the expression of genes encoding eIF5A1, DHPS, or DOHH, and a significant increase in the expression of *EIF5A2* in the striatum of zQ175 heterozygous animals. Overexpression of *EIF5A2* could reflect a response to stalling in HD conditions. It is important to note that the analysis of bulk striatal samples could conceal differences that may be specific to MSSNs.

We next examined the accumulation of eIF5A1 and eIF5A2 proteins and their hypusinated forms by Western-blot. We observed no significant difference in the accumulation of either protein in the striatum of heterozygous zQ175 mice versus corresponding WT controls at 12 months of age (Figure 3B). eIF5A1 and eIF5A2 are 17-kDa proteins with a 84% sequence identity (Clement *et al*, 2006): the stretch spanning from aa 19–88 is identical. We detected a single

17-kDa band using an anti-hypusine antibody (Figure 3B). Some authors have successfully electrophoretically separated eIF5A1 and eIF5A2 (Clement *et al*, 2006). However, we were unable to create any condition in which we could electrophoretically detect mobility differences between these two proteins (Figure 3B). Thus, the single band detected following incubation with the anti-hypusine antibody may contain a mixture of both hypusinated factors, thereby preventing quantification of specific differences in the hypusination of the two isoforms. The high degree of sequence identity shared by both proteins and the insufficient information on the epitope recognized by different commercial antibodies precludes conclusive interpretations regarding the bands detected by the anti-eIF5A1 and anti-eIF5A2 antibodies, and the possibility of cross-reaction cannot be ruled out. Due to these limitations of the Western-blot analysis, it is difficult to extrapolate the observed differences in *eIF5A2* gene expression to protein levels and the degree of hypusination.

Next, we investigated whether there is any differential recruitment of the active (hypusinated) form of eIF5A to ribosomes. We optimized a protocol to prepare polysomal sedimentation gradients: given the low weight of the mouse striatum the protocol was performed using a pool of samples from 4 animals. Figure 4A shows the profiles obtained for the WT and heterozygous zQ175 pools. The peaks corresponding to 40S (small subunit), 60S (large subunit), 80S (monosome), and polysomes are clearly identifiable in the profiles. Analysis of the fractions by Western-blot (Figure 4B) confirmed the expected distribution of ribosomal proteins corresponding to small and large subunits (RPS6 and RPL7), respectively. For both genotypes, most of the hypusinated eIF5A (>80%) was detected in fractions 1 and 2, which do not contain ribosomal subunits. Thus, most of the active stalling relief factor is not associated to ribosomes. This result could be consistent with a transient interaction of the factor with the 60S subunit (Rossi *et al*, 2016), or could be indicative of functions of the eIF5A factor other than facilitating elongation in polyproline-induced stalling, as previously proposed (Saini *et al*, 2009; Schuller & Green, 2018; Schuller *et al*, 2017; Pelechano & Alepuz, 2017). For heterozygous zQ175 mice, we did not detect increased recruitment of the activated factor to

the second half of the gradient, where the stalled polysomes would be expected to sediment (from fraction 7 onwards) (Figure 4B).

Increased accumulation of free 40S ribosomal subunit in the striatum of heterozygous zQ175 animals

The profiles of polysomal sedimentation gradients (Figure 4A) were largely similar for WT and heterozygous zQ175 mice: we observed no apparent differences in the polysomal area that could correspond to the polysomal compaction phenotype observed by ET. It should be noted that due to the nature of the brain samples used it is difficult to obtain optimal clean and concentrated input samples. Consequently, the first part of the gradient contains considerable background signal, and the 40S, 60S and 80S peaks are not fully resolved. The intensity of this background signal varies among the initial fractions and between experiments, precluding comparative quantitative analysis of the profiles to explore differences in the ratios of the different peaks. However, despite this limitation the profiles obtained suggest a higher 40S:80S ratio in heterozygous zQ175 versus WT mice. To confirm this, we analysed fractions from WT and heterozygous mice by Western-blot using anti-RPS6 protein (small subunit) and anti-RPL7 protein (large subunit) antibodies. In these gradients, RPS6 was initially detected in fraction 3 and RPL7 in fraction 4, confirming that fraction 3 exclusively contains 40S subunits. These Western-blots findings confirm that the proportion of free 40S is higher in the heterozygous zQ175 gradient than in the WT gradient (compared the accumulation of RPS6 in fraction 3 to the accumulation of RPS6 and RPL7 in fractions 4 and 5, which mainly contain 60S and 80 subunits) (Figure 4B). Interestingly, the distribution of ribosomal proteins appeared to differ in the polysomal area: in the heterozygous zQ175 gradient we observed a maximum peak in fraction 11 (for both RPS6 and RPL7), while in the WT gradient the proteins were more widely distributed across surrounding fractions, with equivalent levels detected in fractions 10 and 11. Because fractions from these gradients do not have a common quantitative control for normalization, we divided the gradients in two halves and loaded WT and heterozygous samples in the same gel (fractions 1–7 and fractions 7–13). Figure 4C shows a

representative WB of the first half of the gradient. For comparative analysis of protein distribution in WT and heterozygous samples, we calculated the percentage accumulation of each ribosomal protein in a given fraction (100% corresponds to the sum of the intensity for a given protein [RPS6 or RPL7] within each genotype). We performed this analysis in triplicate (three independent Western-blots). Graphs show the mean ± SD percentage accumulation. While the percentage accumulation of RPL7 in both WT and heterozygous samples is very similar, that obtained for RPS6 varied considerably between WT and heterozygous fractions. In fraction 3, there is a significant increase in the percentage accumulation of RPS6 in heterozygous samples in comparison with WT ones. Conversely, in fraction 5, there is a significant decrease in the percentage accumulation of RPS6 in heterozygous samples in comparison with WT ones. This confirms an increase accumulation of free 40S subunit in heterozygous versus WT samples. Figure 4D shows an equivalent analysis for fractions 7–13. For both genotypes the percentage accumulation of RPS6 and RPL7 proteins were very coincident, as expected for fractions containing full ribosomes in different polysomal combinations. However, confirming the observation in Figure 4B, the distribution of ribosomal proteins differed between WT and the heterozygous samples, with maximum accumulation observed in fraction 11 in heterozygous gradients, while a more widely distribution across surrounding fractions occurs in the WT gradients. The relevance of this differential distribution of polysomes and its relation to the architectural phenotype detected by ET remains to be determined.

The expanded CAG repeat does not have a negative effect on protein accumulation

Next we explored whether differences in the ribosomal and polysomal organization observed in the striatum of zQ175 mice models are a direct consequence of mHTT expression. We transfected HEK293T cells with plasmids to overexpress GFP protein fused to the sequence encoded by part of *HTT* exon1 containing either 23 (pEGFP-Q23) or 74 (pEGFP-Q74) CAG repeats, which represent non-pathological and pathological conditions, respectively (Narain *et al*, 1999). Different plasmid concentrations were used (1

μg and 3 μg per well). As a control of transfection, cells were co-transfected with the pNP plasmid (pCMV-NP) (Coloma *et al*, 2009). Results in Figure 5A and 5B show that for both plasmids higher concentrations are associated with greater accumulation of the fusion proteins. This difference may be due to an increase in the percentage transfection (3.5% for 1 μg and 5% for 3 μg) (Figure 5C). Interestingly, at both plasmid concentrations accumulation of the GFP-Q74 fusion protein was greater than that of GFP-Q23 (with a significant effect observed for 3 μg). A similar effect was previously reported (Krauß *et al*, 2013) in transfection experiments using mouse embryonic fibroblasts and plasmids that express 17Q and 49Q tracks in the context of a wider N-terminal HTT fragment (first 500 amino acids). Those authors observed no differences in the expression of mRNAs encoding Q17 and Q49. They also showed that increasing the number of CAG repeats favours binding of the MID1-PP2A-containing translation regulation complex, thus supporting the view that differences in translation efficiency underlie the protein accumulation effect. Our results confirm that this effect is highly dependent on the CAG sequence coding for the polyQ, as the plasmids we used contain the CAG repeat in the context of a partial and short exon 1 sequence (polyQ is flanked in the N- and C-terminus by 10 and 17 aa encoded by exon 1, respectively).

Overexpression of constructs containing CAG repeats in the pathological range is sufficient to induce increased accumulation of free 40S ribosomal subunits

We next explored whether differences in the polysome sedimentation gradients observed in striatal samples from heterozygous zQ175 mice are a direct effect of mHTT expression. We performed polysomal sedimentation gradient analyses using pEFGFP-Q23- and pEGFP-Q74-transfected cells 24 hours post-transfection. This was done applying the modifications described in the Materials and Methods, and therefore the method used differed slightly to that used for striatal samples. As shown in Figure 5D, the gradients from cells overexpressing GFP-Q74 (pathogenic range) revealed changes similar to those observed in striatal samples from heterozygous zQ175 mice. Specifically, we observed a higher percentage of RPS6 accumulation in fractions containing the

40S ribosomal subunit (based on the differential accumulation of ribosomal proteins), confirming that GFP-Q74 overexpression induces increased accumulation of free 40S subunit. Additionally, differences observed in the polysomal area mirrored those detected in gradients of striatal samples. While GFP-Q74-overexpressing cells showed maximum accumulation around fraction 11, ribosomal proteins were more widely distributed across surrounding fractions in GFP-Q23-overexpressing cells.

DISCUSSION

One of the most intriguing characteristics of HD is its slowly progressive nature. While the mutant protein is expressed throughout life, symptoms only begin to manifest at middle age (35-45 years of age), and subsequent life expectancy is 15-20 years. Subtle alterations at the cellular level have been proposed to accumulate overtime, only exerting detrimental effects at later stages (Saudou & Humbert, 2016). Our electron tomography results indicate progressive disturbance of neuronal polysomal architecture in the striatum of the zQ175 mouse model of HD. In this model, motor coordination phenotypes (measured by rotarod performance) and striatal atrophy become evident from 8 months of age (Menalled *et al*, 2012). Interestingly, 8 months was the earliest time point at which rearrangements of polysome structure were evident in our study. This coincidence and the importance of protein synthesis for cellular homeostasis, suggest that the polysomal alterations described here may be relevant to the development of HD-related phenotypes and may reflect disease progression. The protein synthesis disturbances associated with HD (Creus-Muncunill *et al*, 2019; Joag *et al*, 2020; Eshraghi *et al*, 2021) have led some authors to propose that translational dysfunction contributes to the pathogenesis of HD and that new therapies targeting protein synthesis could help alleviate disease symptoms (Joag *et al*, 2020). Our results further underscore the role of translational dysfunction in HD and point to alterations in the architecture of the protein synthesis machinery as a starting point for translational dysfunction.

Studies using gene-specific deletion approaches have enabled the identification of yeast strains in which mHTT toxicity is suppressed (Tauber *et al*, 2011). Interestingly, mHTT overexpression in these strains results in increased

expression of the stalling relief factor *EIF5A2*. The increased *EIF5A2* expression that we detected in the striatum of heterozygous zQ175 animals could represent a cellular response to mHTT toxicity. Increased *EIF5A2* expression together with progressive compaction of polysomes support a scenario of ribosome stalling induced by mHTT. We did not observe increased recruitment of hypusinated eIF5A factor to polysomal fractions in striatal samples from heterozygous zQ175 mice, perhaps implying that a lack of efficient association of eIF5A to polysomes may prevent efficient release of ribosomal stalling. However, it is important to note that both qRT-PCR experiments and polysome sedimentation gradients were performed using whole striatum samples, and this bulk analysis may have masked or underestimated differences specific to MSSN, the neurons most affected in HD.

eIF5A factors are mainly involved in releasing the ribosome stalling induced by the translation of consecutive prolines (Doerfel *et al*, 2013; Gutierrez *et al*, 2013; Ude *et al*, 2013). Interestingly, the polyQ sequence in HTT is followed by a PRD with abundant consecutive prolines. This PRD is present in both WT and mutant HTT, begging the question why stalling induced by the translation of the PRD is only evident in heterozygous animals. An interesting study reported that the dependence of stalling release on eIF5A factors correlates with the translation initiation rate of each particular mRNA (Hersch *et al*, 2014). Thus, when initiation rates are low, translation through polyproline sequences resumes without impeding the progression of upstream ribosomes, even in the absence of eIF5A factors. However, transcripts with a high initiation rate will often engage simultaneously with several ribosomes, which are likely to stall when translating the polyproline sequence and become dependent on the action of eIF5A factors. This is particularly relevant in the context of the findings of Krauß *et al.,* who showed that a higher number of CAG repeats favours binding of the MID1-PP2A-containing translation regulation complex, resulting in more efficient translation (Krauß *et al*, 2013). Together, these findings suggest that mHTT mRNA may be more sensitive to the effect of polyproline-mediated stalling because it is more efficiently translated and therefore more dependent on the action of eIF5A relief factors.

We describe excess accumulation of free 40S subunits in the striatum of the heterozygous zQ175 mouse model of HD. The stability and accumulation of small and large ribosomal subunits are coupled as part of a process that may have evolved to ensure adequate translational performance. An excess of 40S subunits could lead to the formation of translation initiation complexes that cannot be converted to fully translating 80S ribosomes and consequently sequester mRNAs, resulting in general disruption of protein synthesis (Gregory *et al*, 2019). It would be interesting to further investigate the consequences of this excess 40S accumulation on striatal dysfunction in HD and its potential role in the impaired release of ribosome stalling induced by mHTT.

Our findings indicate that changes in the architecture of the protein synthesis machinery may underlie translational alterations associated with HD, thus opening new avenues to better understand the progression of the disease and to facilitate the search for potential therapeutic targets.

Bibliography

Albin RL, Reiner A, Anderson KD, Dure LS, Handelin B, Balfour R, Whetsell WO, Penney JB & Young AB (1992) Preferential loss of striato-external pallidal projection neurons in presymptomatic Huntington's disease. *Ann Neurol* 31: 425–430

Baddeley AJ, Moyeed RA, Howard CV & Boyde A (1993) Analysis of a Three-Dimensional Point Pattern with Replication. *Appl Stat* 42: 641

Bates GP (2005) History of genetic disease: the molecular genetics of Huntington disease - a history. *Nat Rev Genet* 6: 766–773

Bates GP, Dorsey R, Gusella JF, Hayden MR, Kay C, Leavitt BR, Nance M, Ross CA, Scahill RI, Wetzel R, *et al* (2015) Huntington disease. *Nat Rev Dis Primer* 1: 15005

Bhattacharyya A, Thakur AK, Chellgren VM, Thiagarajan G, Williams AD, Chellgren BW, Creamer TP & Wetzel R (2006) Oligoproline effects on polyglutamine conformation and aggregation. *J Mol Biol* 355: 524–535

Brandt F, Carlson L-A, Hartl FU, Baumeister W & Grünewald K (2010) The Three-Dimensional Organization of Polyribosomes in Intact Human Cells. *Mol Cell* 39: 560–569

Brandt F, Etchells SA, Ortiz JO, Elcock AH, Hartl FU & Baumeister W (2009) The Native 3D Organization of Bacterial Polysomes. *Cell* 136: 261–271

Caron NS, Dorsey ER & Hayden MR (2018) Therapeutic approaches to Huntington disease: from the bench to the clinic. *Nat Rev Drug Discov* 17: 729–750

Chu J, Hong NA, Masuda CA, Jenkins BV, Nelms KA, Goodnow CC, Glynne RJ, Wu H, Masliah E, Joazeiro CAP, *et al* (2009) A mouse forward genetics screen identifies LISTERIN as an E3 ubiquitin ligase involved in neurodegeneration. *Proc Natl Acad Sci* 106: 2097–2103

Clement PMJ, Johansson HE, Wolff EC & Park MH (2006) Differential expression of eIF5A-1 and eIF5A-2 in human cancer cells. *FEBS J* 273: 1102–1114

Coloma R, Valpuesta JM, Arranz R, Carrascosa JL, Ortín J & Martín-Benito J (2009) The Structure of a Biologically Active Influenza Virus Ribonucleoprotein Complex. *PLoS Pathog* 5: e1000491

Creus-Muncunill J, Badillos-Rodríguez R, Garcia-Forn M, Masana M, Garcia-Díaz Barriga G, Guisado-Corcoll A, Alberch J, Malagelada C, Delgado-García JM, Gruart A, *et al* (2019) Increased translation as a novel pathogenic mechanism in Huntington's disease. *Brain* 142: 3158–3175

Darnell JC (2014) Ribosome rescue and neurodegeneration. *Science* 345: 378–379

Dehay B & Bertolotti A (2006) Critical role of the proline-rich region in Huntingtin for aggregation and cytotoxicity in yeast. *J Biol Chem* 281: 35608–35615

Díaz-López I, Toribio R, Berlanga JJ & Ventoso I (2019) An mRNA-binding channel in the ES6S region of the translation 48S-PIC promotes RNA unwinding and scanning. *eLife* 8: e48246

Diggle PJ (2013) Statistical Analysis of Spatial and Spatio-Temporal Point Patterns 0 ed. Chapman and Hall/CRC

Doerfel LK, Wohlgemuth I, Kothe C, Peske F, Urlaub H & Rodnina MV (2013) EF-P Is Essential for Rapid Synthesis of Proteins Containing Consecutive Proline Residues. *Science* 339: 85–88

Duennwald ML, Jagadish S, Muchowski PJ & Lindquist S (2006) Flanking sequences profoundly alter polyglutamine toxicity in yeast. *Proc Natl Acad Sci U S A* 103: 11045–11050

Eshraghi M, Karunadharma PP, Blin J, Shahani N, Ricci EP, Michel A, Urban NT, Galli N, Sharma M, Ramírez-Jarquín UN, *et al* (2021) Mutant Huntingtin stalls ribosomes and represses protein synthesis in a cellular model of Huntington disease. *Nat Commun* 12: 1461

Fernandez J-J (2012) Computational methods for electron tomography. *Micron* 43: 1010–1030

Fernandez-Fernandez MR, Ferrer I & Lucas JJ (2011) Impaired ATF6α processing, decreased Rheb and neuronal cell cycle re-entry in Huntington's disease. *Neurobiol Dis* 41: 23–32

Fernandez-Fernandez MR, Ruiz-Garcia D, Martin-Solana E, Chichon FJ, Carrascosa JL & Fernandez J-J (2017) 3D electron tomography of brain tissue unveils distinct Golgi structures that sequester cytoplasmic contents in neurons. *J Cell Sci*: jcs.188060

Frank J ed. (2006) Electron Tomography New York, NY: Springer New York

Gao F-B, Richter JD & Cleveland DW (2017) Rethinking Unconventional Translation in Neurodegeneration. *Cell* 171: 994–1000

Gregory B, Rahman N, Bommakanti A, Shamsuzzaman M, Thapa M, Lescure A, Zengel JM & Lindahl L (2019) The small and large ribosomal subunits depend on each other for stability and accumulation. *Life Sci Alliance* 2: e201800150

Gutierrez E, Shin B-S, Woolstenhulme CJ, Kim J-R, Saini P, Buskirk AR & Dever TE (2013) eIF5A Promotes Translation of Polyproline Motifs. *Mol Cell* 51: 35–45

He W & Fernández J-J (2010) Electron Tomography. In *Encyclopedia of Life Sciences*, John Wiley & Sons, Ltd (ed) p a0021877. Chichester, UK: John Wiley & Sons, Ltd

Heiman M, Schaefer A, Gong S, Peterson JD, Day M, Ramsey KE, Suárez-Fariñas M, Schwarz C, Stephan DA, Surmeier DJ, *et al* (2008) A Translational

Profiling Approach for the Molecular Characterization of CNS Cell Types. *Cell* 135: 738–748

Hersch SJ, Elgamal S, Katz A, Ibba M & Navarre WW (2014) Translation Initiation Rate Determines the Impact of Ribosome Stalling on Bacterial Protein Synthesis. *J Biol Chem* 289: 28160–28171

Ishimura R, Nagy G, Dotu I, Zhou H, Yang X-L, Schimmel P, Senju S, Nishimura Y, Chuang JH & Ackerman SL (2014) Ribosome stalling induced by mutation of a CNS-specific tRNA causes neurodegeneration. *Science* 345: 455–459

Joag H, Ghatpande V, Desai M, Sarkar M, Raina A, Shinde M, Chitale R, Deo A, Bose T & Majumdar A (2020) A role of cellular translation regulation associated with toxic Huntingtin protein. *Cell Mol Life Sci* 77: 3657–3670

Kapur M & Ackerman SL (2018) mRNA Translation Gone Awry: Translation Fidelity and Neurological Disease. *Trends Genet* 34: 218–231

Kapur M, Monaghan CE & Ackerman SL (2017) Regulation of mRNA Translation in Neurons—A Matter of Life and Death. *Neuron* 96: 616–637

Krauß S, Griesche N, Jastrzebska E, Chen C, Rutschow D, Achmüller C, Dorn S, Boesch SM, Lalowski M, Wanker E, *et al* (2013) Translation of HTT mRNA with expanded CAG repeats is regulated by the MID1–PP2A protein complex. *Nat Commun* 4: 1511

Kremer JR, Mastronarde DN & McIntosh JR (1996) Computer Visualization of Three-Dimensional Image Data Using IMOD. *J Struct Biol* 116: 71–76

Kwon D (2021) Failure of genetic therapies for Huntington's devastates community. *Nature* 593: 180–180

Livak KJ & Schmittgen TD (2001) Analysis of Relative Gene Expression Data Using Real-Time Quantitative PCR and the 2−ΔΔCT Method. *Methods* 25: 402–408

Mahamid J, Pfeffer S, Schaffer M, Villa E, Danev R, Kuhn Cuellar L, Forster F, Hyman AA, Plitzko JM & Baumeister W (2016) Visualizing the molecular sociology at the HeLa cell nuclear periphery. *Science* 351: 969–972

Matamales M, Bertran-Gonzalez J, Salomon L, Degos B, Deniau J-M, Valjent E, Hervé D & Girault J-A (2009) Striatal Medium-Sized Spiny Neurons: Identification by Nuclear Staining and Study of Neuronal Subpopulations in BAC Transgenic Mice. *PLoS ONE* 4: e4770

Melnikov S, Mailliot J, Rigger L, Neuner S, Shin B, Yusupova G, Dever TE, Micura R & Yusupov M (2016) Molecular insights into protein synthesis with proline residues. *EMBO Rep* 17: 1776–1784

Menalled LB, Kudwa AE, Miller S, Fitzpatrick J, Watson-Johnson J, Keating N, Ruiz M, Mushlin R, Alosio W, McConnell K, *et al* (2012) Comprehensive behavioral and molecular characterization of a new knock-in mouse model of Huntington's disease: zQ175. *PloS One* 7: e49838

Meriin AB, Zhang X, Alexandrov IM, Salnikova AB, Ter-Avanesian MD, Chernoff YO & Sherman MY (2007) Endocytosis machinery is involved in aggregation of proteins with expanded polyglutamine domains. *FASEB J Off Publ Fed Am Soc Exp Biol* 21: 1915–1925

Narain Y, Wyttenbach A, Rankin J, Furlong RA & Rubinsztein DC (1999) A molecular investigation of true dominance in Huntington's disease. *J Med Genet* 36: 739–746

Nielsen H ed. (2011) RNA: methods and protocols New York: Humana Press

Nixon, Mark S. & Aguado, Alberto S. (2020) Feature Extraction and Image Processing for Computer Vision Elsevier

Nowogrodzki A (2018) Huntington's disease: 4 big questions. *Nature* 557: S48

Park MH, Cooper HL & Folk JE (1981) Identification of hypusine, an unusual amino acid, in a protein from human lymphocytes and of spermidine as its biosynthetic precursor. *Proc Natl Acad Sci* 78: 2869–2873

Pavlov MY, Watts RE, Tan Z, Cornish VW, Ehrenberg M & Forster AC (2009) Slow peptide bond formation by proline and other N-alkylamino acids in translation. *Proc Natl Acad Sci* 106: 50–54

Pelechano V & Alepuz P (2017) eIF5A facilitates translation termination globally and promotes the elongation of many non polyproline-specific tripeptide sequences. *Nucleic Acids Res* 45: 7326–7338

Pringle ES, McCormick C & Cheng Z (2019) Polysome Profiling Analysis of mRNA and Associated Proteins Engaged in Translation. *Curr Protoc Mol Biol* 125: e79

Ripley BD (1988) Statistical Inference for Spatial Processes 1st ed. Cambridge University Press

Ross CA & Tabrizi SJ (2011) Huntington's disease: from molecular pathogenesis to clinical treatment. *Lancet Neurol* 10: 83–98

Rossi D, Barbosa NM, Galvão FC, Boldrin PEG, Hershey JWB, Zanelli CF, Fraser CS & Valentini SR (2016) Evidence for a Negative Cooperativity between eIF5A and eEF2 on Binding to the Ribosome. *PLOS ONE* 11: e0154205

Saini P, Eyler DE, Green R & Dever TE (2009) Hypusine-containing protein eIF5A promotes translation elongation. *Nature* 459: 118–121

Saudou F & Humbert S (2016) The Biology of Huntingtin. *Neuron* 89: 910–926

Schaffer M, Pfeffer S, Mahamid J, Kleindiek S, Laugks T, Albert S, Engel BD, Rummel A, Smith AJ, Baumeister W, *et al* (2019) A cryo-FIB lift-out technique enables molecular-resolution cryo-ET within native Caenorhabditis elegans tissue. *Nat Methods* 16: 757–762

Schmidt C, Becker T, Heuer A, Braunger K, Shanmuganathan V, Pech M,

Berninghausen O, Wilson DN & Beckmann R (2016) Structure of the hypusinylated eukaryotic translation factor eIF-5A bound to the ribosome. *Nucleic Acids Res* 44: 1944–1951

Schuller AP & Green R (2018) Roadblocks and resolutions in eukaryotic translation. *Nat Rev Mol Cell Biol* 19: 526–541

Schuller AP, Wu CC-C, Dever TE, Buskirk AR & Green R (2017) eIF5A Functions Globally in Translation Elongation and Termination. *Mol Cell* 66: 194-205.e5

Tabrizi SJ, Ghosh R & Leavitt BR (2019) Huntingtin Lowering Strategies for Disease Modification in Huntington's Disease. *Neuron* 101: 801–819

Tartari M, Gissi C, Lo Sardo V, Zuccato C, Picardi E, Pesole G & Cattaneo E (2008) Phylogenetic comparison of huntingtin homologues reveals the appearance of a primitive polyQ in sea urchin. *Mol Biol Evol* 25: 330–338

Tauber E, Miller-Fleming L, Mason RP, Kwan W, Clapp J, Butler NJ, Outeiro TF, Muchowski PJ & Giorgini F (2011) Functional Gene Expression Profiling in Yeast Implicates Translational Dysfunction in Mutant Huntingtin Toxicity. *J Biol Chem* 286: 410–419

The Huntington's Disease Collaborative Research Group (1993) A novel gene containing a trinucleotide repeat that is expanded and unstable on Huntington's disease chromosomes. *Cell* 72: 971–983

Ude S, Lassak J, Starosta AL, Kraxenberger T, Wilson DN & Jung K (2013) Translation Elongation Factor EF-P Alleviates Ribosome Stalling at Polyproline Stretches. *Science* 339: 82–85

Vonsattel J-P, Myers RH, Stevens TJ, Ferrante RJ, Bird ED & Richardson EP (1985) Neuropathological Classification of Huntington's Disease: *J Neuropathol Exp Neurol* 44: 559–577

Wohlgemuth I, Brenner S, Beringer M & Rodnina MV (2008) Modulation of the Rate of Peptidyl Transfer on the Ribosome by the Nature of Substrates. *J Biol Chem* 283: 32229–32235

Wu G-Q, Xu Y-M & Lau ATY (2020) Recent insights into eukaryotic translation initiation factors 5A1 and 5A2 and their roles in human health and disease. *Cancer Cell Int* 20: 142

Yang J, Hao X, Cao X, Liu B & Nyström T (2016) Spatial sequestration and detoxification of Huntingtin by the ribosome quality control complex. *eLife* 5: e11792

Acknowledgements

We thank Pablo Sola Alarcón for valuable technical assistance. We would also like to thank Eber Martínez and all staff at the Animal Facility of the Centro Nacional de Biotecnología (CNB-CSIC, Madrid) for their work over the years. qPCR experiments were conducted at the Genomics and NGS Core Facility at the Centro de Biología Molecular Severo Ochoa, which is part of the CEI UAM+CSIC, Madrid. HPF and FS experiments together with the observation of brain sections were performed in the Electron Microscopy Facility at the CNB-CSIC. The acquisition of tilt series for tomography was performed in the Cryoelectron Microscopy Facility at CNB-CSIC. We are profoundly grateful to the Fundación Ramón Areces for the grant that made this work possible, and to AEI/FEDER (SAF2017-84565-R) for additional funding.

Author Contributions

(CRediT: https://onlinelibrary.wiley.com/doi/epdf/10.1002/leap.1210)

EMS: Investigation, Validation, Formal Analysis, Methodology, Writing - Original draft .

IDL: Investigation, Resources, Writing - Review & Editing.

IV: Investigation, Resources, Writing - Review & Editing.

JJF: Conceptualization, Methodology, Software, Investigation, Formal Analysis, Writing - Original draft, Funding Acquisition.

MRFF: Conceptualization, Methodology, Investigation, Validation, Formal Analysis, Writing - Original draft, Funding Acquisition.

Conflict of interest

The authors declare that they have no conflict of interest in relation to this manuscript.

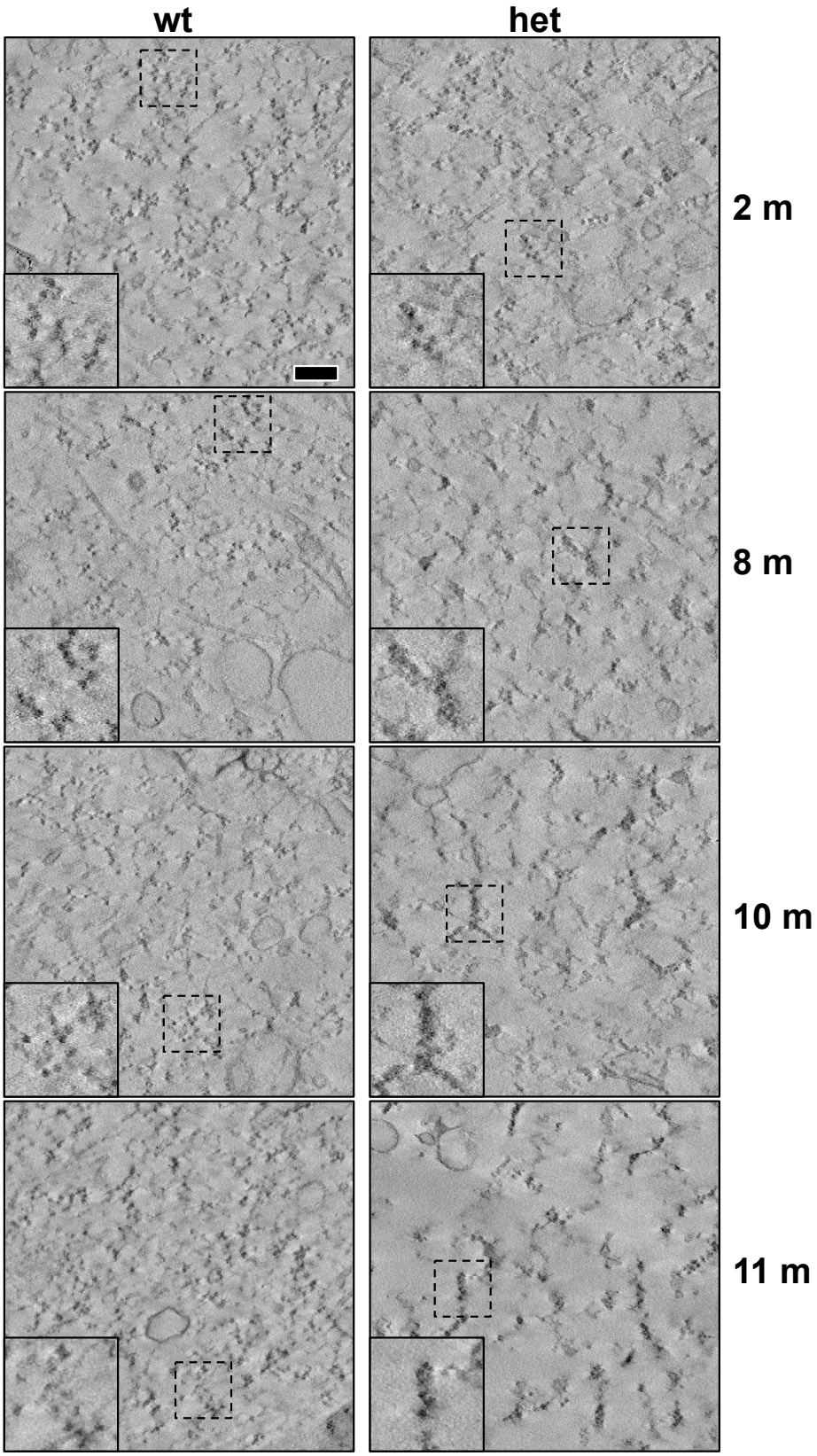

Figure 1. Progressive alterations in ribosomal/polysomal architecture in HD observed with ET. Slices of tomograms from wild-type (WT) (left) and heterozygous (het) zQ175 mice (right). From top to bottom, images correspond to mice aged 2, 8, 10, and 11 months. Insets are magnified views of dashed-line boxes. Scale bar: 200 nm.

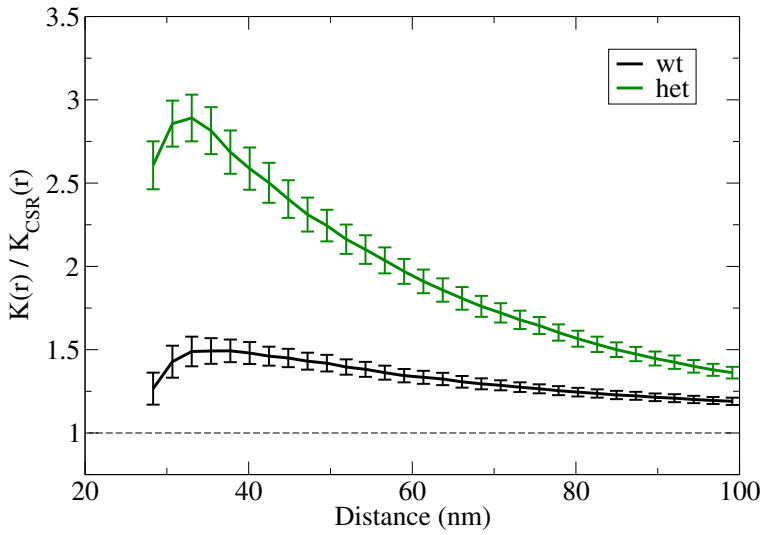

Figure 2. Second-order spatial pattern analysis based on Ripley's K function. Ripley's K-function relative to a random distribution, $K(r)/K_{CSR}(r)$ as a function of the distance calculated for tomograms from different neurons in heterozygous zQ175 (n=6) and WT mice (n=5) at age 11 months. The plot depicts mean values and the standard error. This plot represents the expected number of ribosomes within a distance r around a random ribosome *(K(r)),* relative to the expected value in a random distribution ($K_{CSR}(r)$). Values >1 indicate clustering.

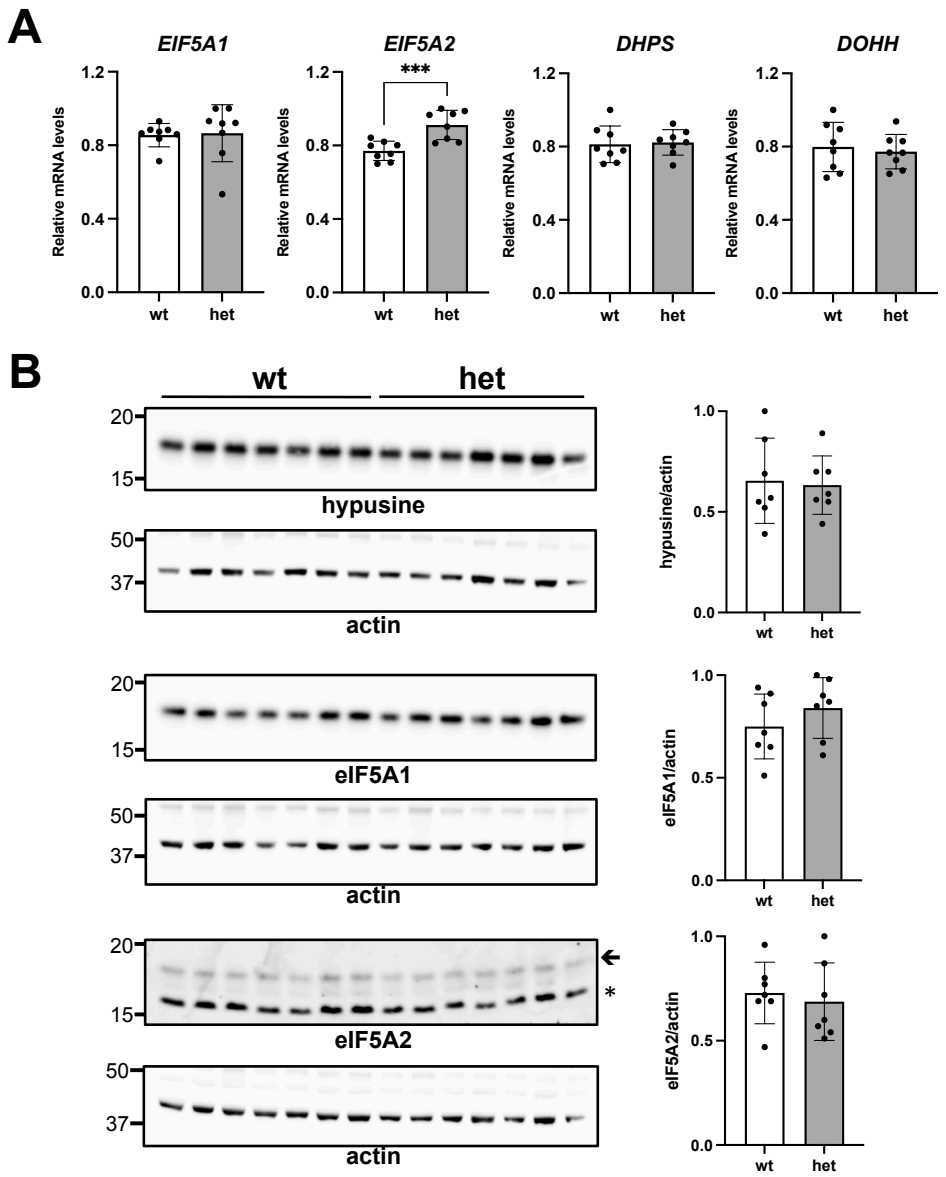

Figure 3. *EIF5A2* stalling relief factor is overexpressed in the striatum of heterozygous zQ175 mice. (A) Relative accumulation of *EIF5A1*, *EIF5A2*, *DHPS* and *DOHH* mRNA in the striatum of heterozygous zQ175 mice and WT controls analysed by qRT-PCR. Data are normalized to expression levels of the reference gene *YWHAZ*. For each independent gene the highest value after normalization to *YWHAZ* was set to 1 to facilitate comparisons. Data followed a normal distribution (Shapiro-Wilk test) with the exception of *EIF5A1*. No significant difference between groups was observed for *EIF5A1, DHPS,* or *DOHH* gene expression (p=0.2786, 0.8130, and 0.6642, respectively). *EIF5A2* expression was significantly increased in heterozygous zQ175 mice versus controls (p=0.0009). Data are presented as the mean ± SD (n=8). **(B)** Western-blot analysis of the accumulation of hypusinated eIF5A factor, eIF5A1, and eIF5A2 in the striatum of 12-month-old heterozygous zQ175 mice and WT controls. Actin was used as a loading control to quantify relative accumulation (shown on the right). In all cases data followed a normal distribution. There was no significant difference between groups in the accumulation of any of the factors studied (p=0.8289, 0.2983, and 0.6520, respectively). Data are presented as the mean ± SD (n=7). Arrow in eIF5A2 blot indicates the expected band corresponding to full-length eIF5A2. Asterisk indicates a very prominent band that may represent a degradation product of

eIF5A2.

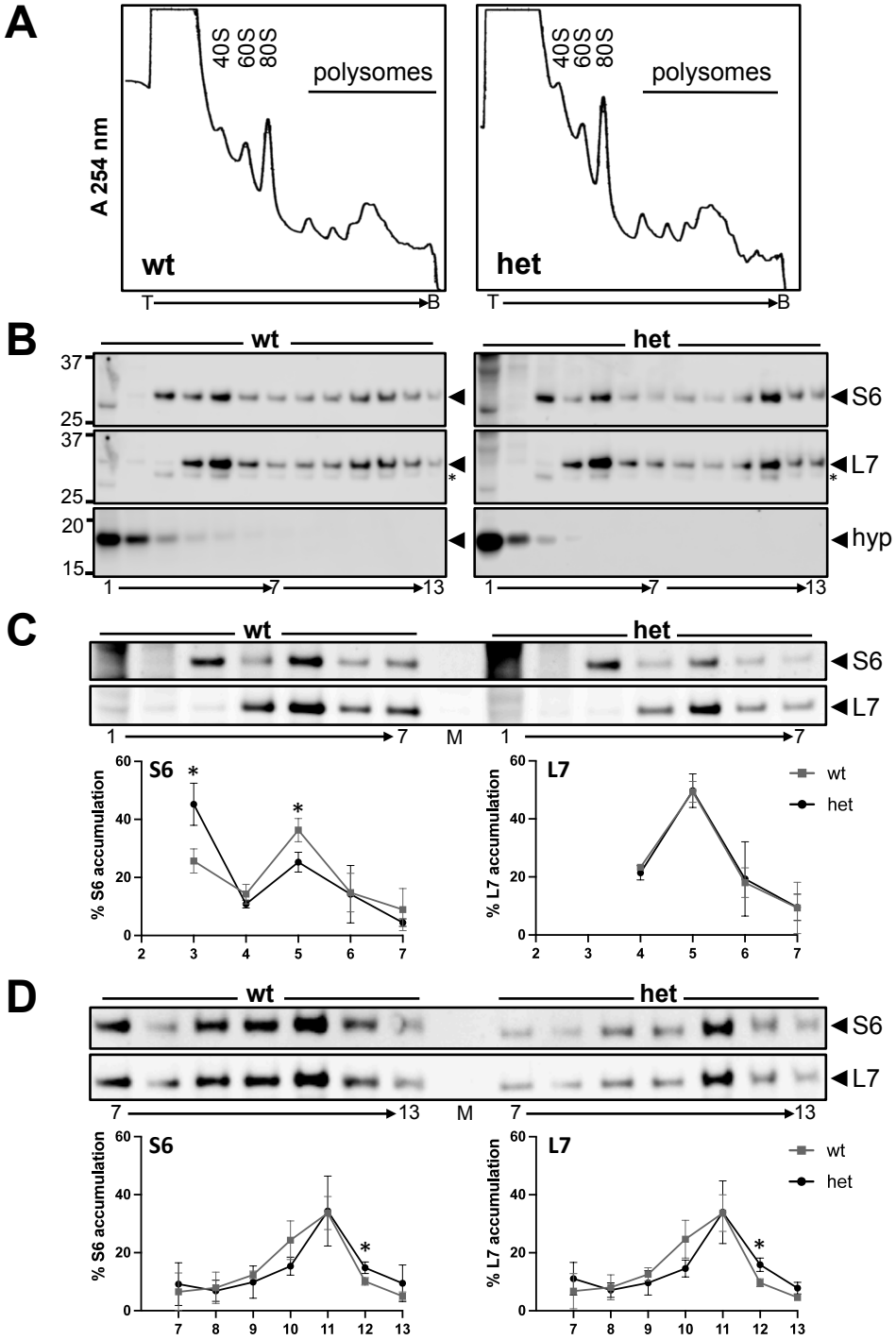

Figure 4. Polysomal sedimentation gradients generated from striatal samples from 9-month-old WT and heterozygous zQ175 mice. (A) Profiles obtained by continuous monitoring of absorbance at 254 nm. Peaks corresponding to 40S, 60S, 80S, and polysomes are identifiable. On the X axis, T indicates the top and B the bottom of the gradient (continuous 10-50% sucrose gradient). **(B)** Accumulation of ribosomal proteins RPS6 (S6) (small subunit) and RPL7 (L7) (large subunit) and hypusinated eIF5A factor in gradient fractions by Western-blot. Fraction 1 corresponds to the top and fraction 13 to the bottom of the gradient. The proportion of free 40S (represented by the accumulation of RPS6 in fraction 3) appears higher in the

gradients from heterozygous zQ175 mice. The distribution of ribosomal proteins in the polysomal fractions differs slightly between genotypes. Most hypusinated eIF5A (>80%) accumulates in the first two fractions that do not contain ribosomal subunits (soluble fractions). Asterisks indicate the residual signal of RPS6. **(C)** To compare the relative accumulation of ribosomal proteins in gradients from WT and heterozygous zQ175 striatal samples, fractions 1 to 7 for each genotype were loaded in the same gel. To compensate for the absence of an internal quantity control, three independent gels were loaded with the same fractions. The percentage accumulation was calculated for each protein and genotype independently. The sum of the intensities of a given protein in a given genotype was set at 100%. Fractions 1 and 2 (for RPS6) and fractions 1, 2 and 3 (for RPL7) were not quantified as they did not accumulate a significant amount of the corresponding protein and displayed a high level of background signal. Graphs show the mean ± SD percentage accumulation for each fraction. The percentage accumulation of the RPL7 protein (right panel) overlaps considerably in the WT and heterozygous fractions. However, the percentage accumulation of the RPS6 protein (left panel) differs substantially between genotypes. Quantification confirmed a significant increase in the percentage of RPS6 protein in heterozygous fraction 3 (containing free 40S subunit) ($p=0.0156$), while a corresponding decrease in the percentage of RPS6 was observed in fraction 5 ($p=0.0223$) (mainly containing 80S subunits). **(D)** The relative accumulation of ribosomal proteins in fractions 7 to 13, was compared by loading the corresponding fractions and quantifying as described in **C**. For each genotype, similar levels of accumulation were observed for RPS6 and RPL7. In heterozygous zQ175 mice, significant increases in the percentage accumulation of RPS6 and RPL7 were observed in fraction 12 ($p=0.0265$ and $p=0.0164$, respectively) as compared with WT. There were also increases in the percentage accumulation of RPS6 and RPL7 in WT fraction 10, although this effect did not reach statistical significance ($p=0.1038$ and $p=0.0708$, respectively). In **C** and **D,** the channel in which the molecular weight markers were loaded is indicated with the letter M.

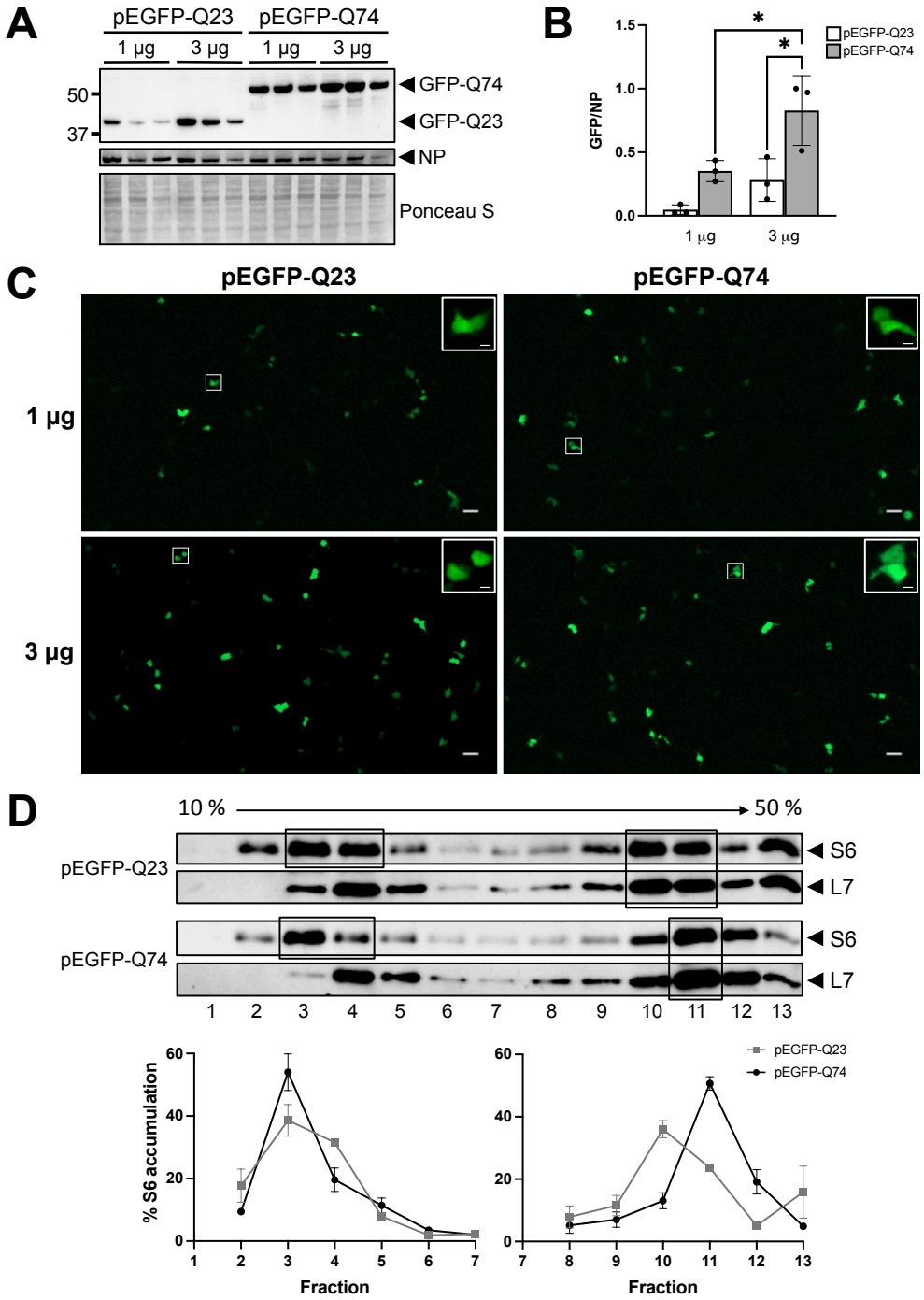

Figure 5. Transfection of HEK293T cells with plasmids expressing a GFP fusion protein containing part of the exon1 *HTT* coding sequence including 23Q or 74Q. (A) Western-blot analysis of the accumulation of fusion proteins GFP-Q23 and GFP-Q74 18 hours post-transfection with different amounts of plasmids pEGFP-Q23 and pEGFP-Q74 (1 or 3 µg per well). A band of the expected size was detected for each fusion protein. A plasmid expressing the NP protein was co-transfected for quantification purposes. The accumulation of NP protein is shown in the second panel.

The third panel shows the membrane staining with Ponceau S. Samples were run in triplicate. **(B)** Quantification of the relative accumulation of GFP-Q23 and GFP-Q74 for the different transfection conditions shown in **A**. Mean ± SD values are shown. Increased accumulation of GFP-Q74 was observed at both plasmid concentrations: this effect was significant at 3 μg (p=0.0422) but not at 1 μg (p=0.1000). For both plasmids an increase in the amount of transfected plasmid was associated with increased accumulation of the fusion protein. This increase was not significant for GFP-Q23 (p=0.1000) but was for GFP-Q74 (p=0.0453). The pEGFP-Q23 1 μg dataset showed a non-normal distribution, all other groups had a normal distribution. **C)** Fluorescence images to detect the accumulation of GFP fusion proteins by GFP fluorescence were taken on culture plates using a Leica DMI6000B microscope at 10x magnification. Zoom images (insets) show that only soluble GFP fusion proteins accumulate at this time-point post-transfection. The percentages of transfection were as follows: 3.4% for pEGFP-Q23-1 μg, 3.5% for pEGFP-Q74-1 μg, 5.4% for pEGFP-Q23-3 μg, and 5% for pEGFP-Q74-3 μg. Scale bar: 50 μm for main panels and 10 μm for insets. **(D)** Western-blot analysis of fractions from polysomal sedimentation gradients obtained from HEK293T cells transfected with either pEFGP-Q23 or pEGFP-Q74. Cells were recovered 24 hours post-transfection and the percentage of transfection was 20-25%. Boxes on the left highlight the differential accumulation of RPS6 (small ribosomal subunit) in the first fractions of the gradient. Overexpression of the fusion protein containing 74Q was associated with increased percentage of free 40S subunits. Boxes on the right highlight the differential accumulation of polysomes in the mid polysomal area between pEGFP-Q23 and pEGFP-Q74 transfected cells. Bottom graphs show the percentage accumulation of RPS6 protein in the different fractions to highlight differences. Two sets of equivalent Western-blots were run to compensate for the absence of a shared internal loading control. Graphs depict the mean percentage ± SEM.

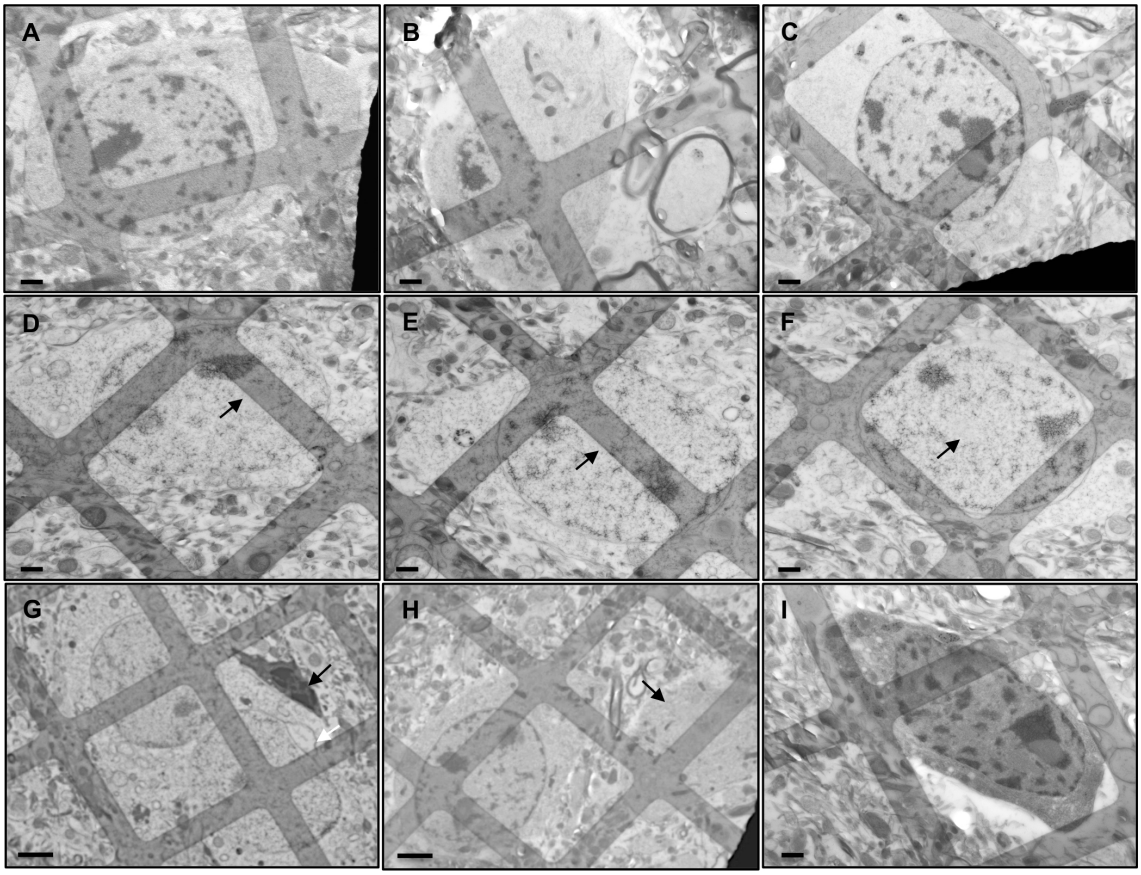

Figure EV1. Representative EM images of striatal cells from 250-nm-thick sections of brain tissue. (A-F) Cells compatible with medium-sized spiny neurons (MSSN) based on morphological criteria in WT control **(A-C)** and heterozygous zQ175 **(D-F)** mice aged 11 months. In the HD model, these cells appear paler, an effect evident in the chromatin, nucleus and cytoplasm. In addition, nuclear inclusions are identifiable in the HD model (arrows in D-F). **(G)** A cell, likely microglia, with nucleus and cytoplasm that are highly dense (black arrow) is observed near two pale cells compatible with MSSNs. One of these MSSNs contains a nuclear bleb (white arrow), which are often found in HD neurons and are indicative of neurodegeneration. **(H)** A putative MSSN and, on the right, an area of cytoplasm from another cell (arrow) with a similar appearance but not showing the nucleus. **(I)** A cell from a control animal, with size and morphology compatible with a MSSN, with highly dense nucleus and cytoplasm (signs of cell death). Scale bars: 1 µm (A-F, I), 2 µm (G-H).

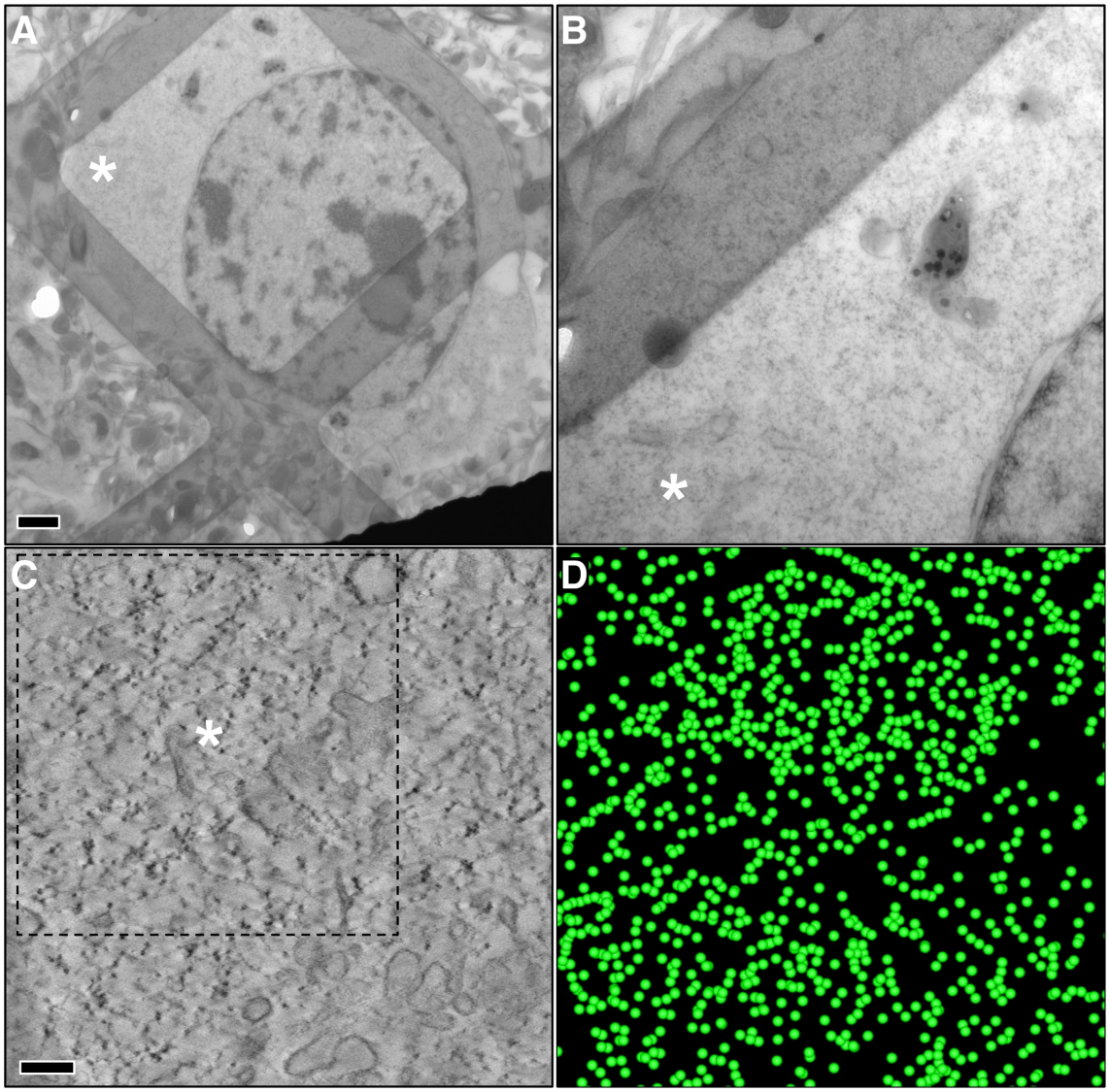

Figure EV2. Electron tomography of a striatal neuron from a 250 nm thick section of brain tissue from an 11-month-old wild-type mouse. (A) Image from conventional 2D electron microscopy, showing the nucleus of the neuron and cytoplasm. Scale bar: 1 µm. **(B)** Magnified view from the area marked by the asterisk in **A**. **(C)** Tomogram slice computed from a tilt-series acquired at the position marked with the asterisk in **B**. The individual ribosomes are clearly identifiable as black dots in the spotty cytoplasm. The cytoplasm is crowded by numerous ribosomes, and polysomal clusters are also observed. Scale bar: 200 nm. **(D)** 3D visualization of the ribosomes detected using our automated procedure based on Laplacian of Gaussian (LoG) and represented by green spheres. These ribosomes correspond to the area outlined with a dashed line in **C**.

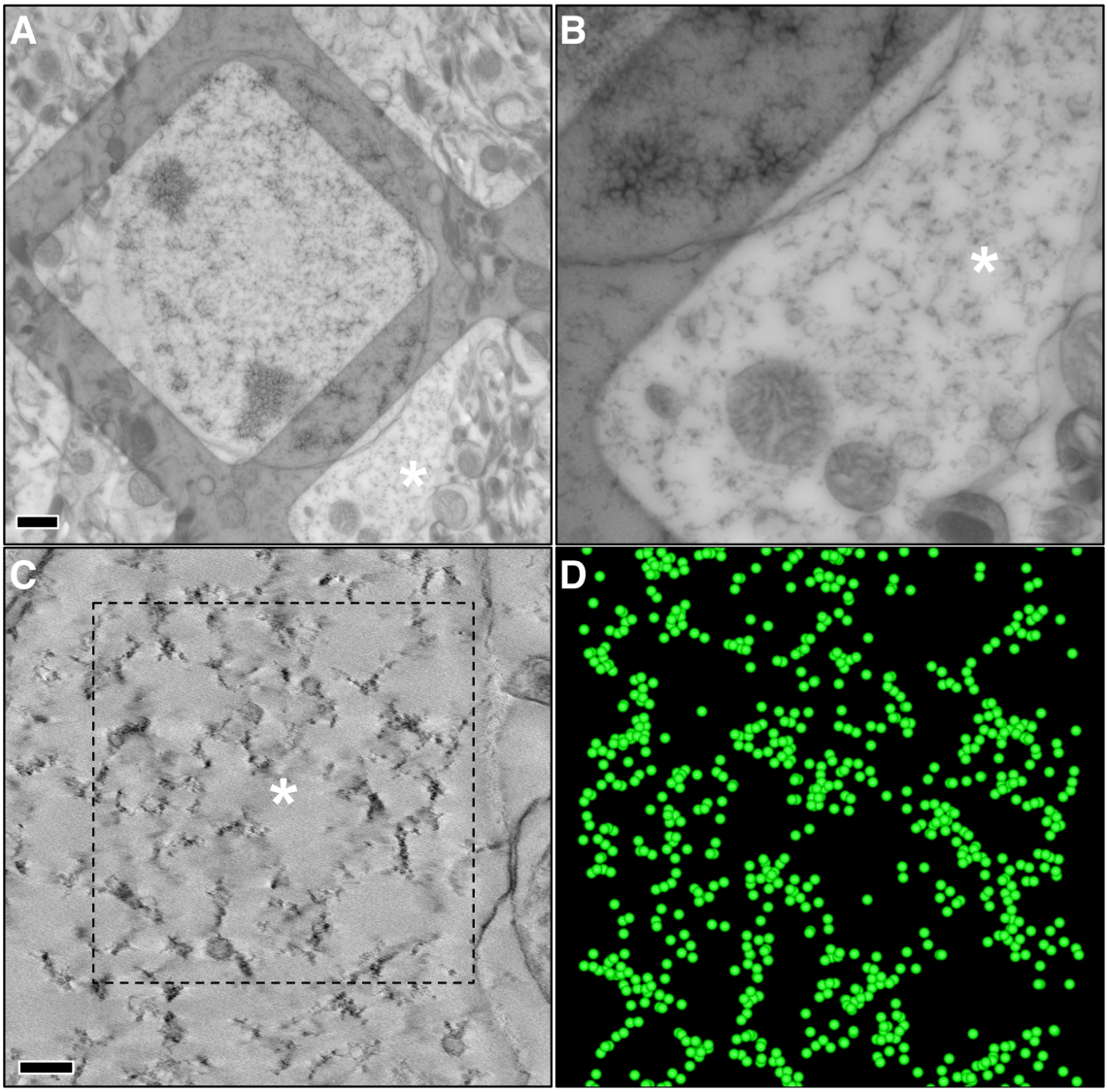

Figure EV3. Electron tomography of a striatal neuron from a 250-nm-thick section of brain tissue from an 11-month-old heterozygous zQ175 mouse. (A-D) Interpretation of the panels as described in Figure EV2. In this case, few individual ribosomes are observed in the tomogram (C). Instead, tightly-coupled clusters of ribosomes are evident, and there is substantial empty cytoplasmic space among the clusters.

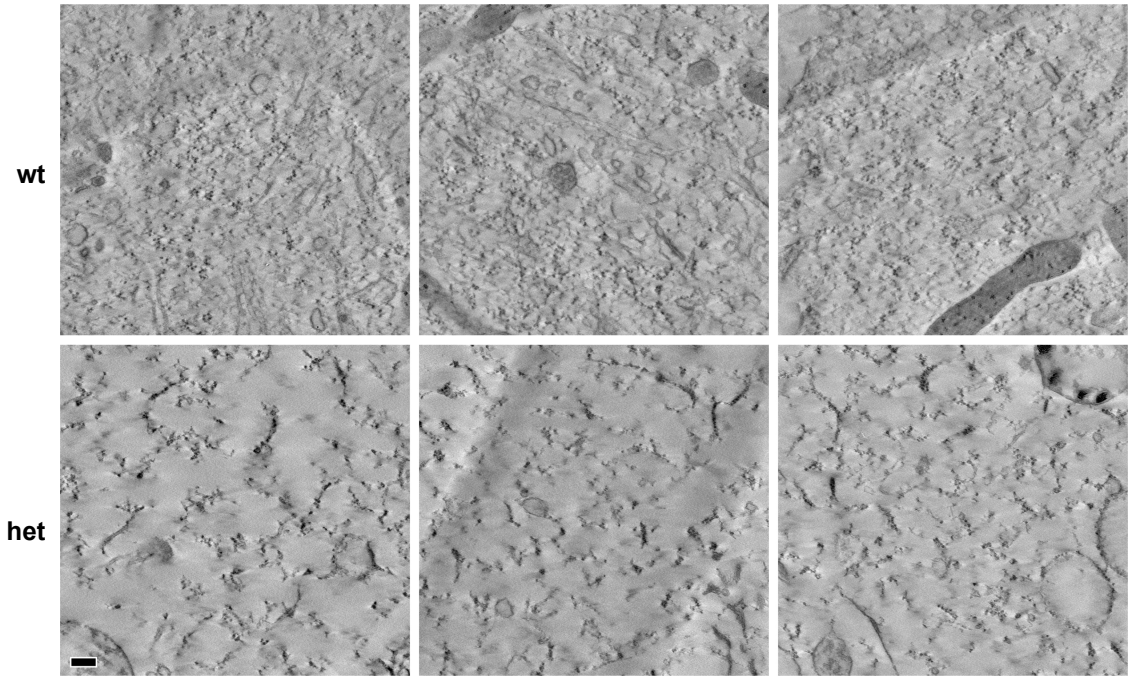

Figure EV4. Representative slices of tomograms from 11-month-old wild-type control (top) and heterozygous zQ175 (bottom) mice. Scale bar: 200 nm.

Supplementary Figures

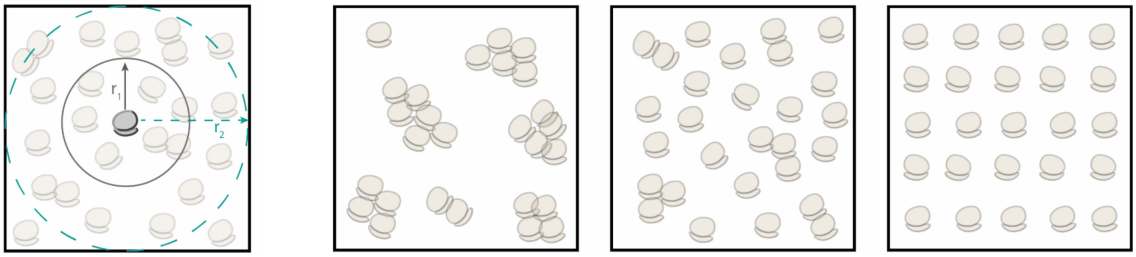

Ripley's K function | $K(r)/K_{CSR}(r) > 1$ | $K(r)/K_{CSR}(r) = 1$ | $K(r)/K_{CSR}(r) < 1$

Figure S1. Ripley's K function and spatial distribution patterns. Left: Ripley's K function is calculated at a range of distances *r* and measures the expected number of ribosomes within the distance *r* from an arbitrary ribosome, normalized by the density of the ribosome distribution. In this study, the K function has been implemented in 3D, though for simplicity the sketch depicts 2D. Right: Three main spatial distribution patterns can be identified when comparing the actual K function with the expected value under complete spatial randomness (K_{CSR}): clustering ($K(r)/K_{CSR}(r) > 1$); randomness ($K(r)/K_{CSR}(r) = 1$); and regularity or dispersion ($K(r)/K_{CSR}(r) < 1$).

Supplementary Tables

Table 1. Primers used for qRT-PCR of target genes of interest

Gene	ENSEMBL	Primer	Sequence 5'- 3'	Amplicon size
eIF5A1	ENSMUSG00000078812	Fw[1]	GGATGTCCCCAACATCAAAC	75 bp
		Rv[2]	TCCTGGAGCAGGGATAGGTA	
eIF5A2	ENSMUSG00000050192	Fw	GCAAAATCGTGGAGATGTCA	127 bp
		Rv	TCCATGTTGTGAGTAGAAGGACA	
DHPS	ENSMUSG00000060038	Fw	TACCTCGTGCAGCACAACA	102 bp
		Rv	GAACTCGCCAAGGTATGTGG	
DOHH	ENSMUSG00000078440	Fw	CCGGGCCCTGTTTACACT	60 bp
		Rv	CGGCTGATCCACGAGATAG	

[1]Fw: forward primer
[2]Rv: reverse primer

Table 2. Primers used for amplification by qRT-PCR of reference genes for normalization

Gene	Primer	Sequence 5 '- 3'	Amplicon size
18S	Fw[1]	CTCAACACGGGAAACCTCAC	110 bp
	Rv[2]	CGCTCCACCAACTAAGAACG	
BACT	Fw	CTAAGGCCAACCGTGAAAAG	104 bp
	Rv	ACCAGAGGCATACAGGGACA	
B2M	Fw	TACATACGCCTGCAGAGTTAAGCA	76 bp
	Rv	TGATCACATGTCTCGATCCCAG	
GAPDH	Fw	CACCACCAACTGCTTAGCCC	76 bp
	Rv	TGTGGTCATGAGCCCTTCC	
YWHAZ	Fw	TTACTTGGCCGAGGTTGCT	60 bp
	Rv	TGCTGTGACTGGTCCACAAT	

[1]Fw: forward primer
[2]Rv: reverse primer